Precessing Vortex Motion and Instability in a Rotating Column of Superfluid ^{3}He-B

R. Hänninen,[1] V.B. Eltsov,[1,2] A.P. Finne,[1] R. de Graaf,[1] J. Kopu,[1] M. Krusius,[1] and R.E. Solntsev[1]

[1] *Low Temperature Laboratory, Helsinki University of Technology, P.O.Box 5300, 02015 HUT, Finland*
[2] *Kapitza Institute for Physical Problems, Kosygina 2, 119334 Moscow, Russia*

(Dated: October 1, 2008)

The flow of quantized vortex lines in superfluid ^{3}He-B is laminar at high temperatures, but below $0.6\,T_c$ turbulence becomes possible, owing to the rapidly decreasing mutual friction damping. In the turbulent regime a vortex evolving in applied flow may become unstable, create new vortices, and start turbulence. We monitor this single-vortex instability with NMR techniques in a rotating cylinder. Close to the onset temperature of turbulence, an oscillating component in NMR absorption has been observed, while the instability generates new vortices at a low rate ~ 1 vortex/s, before turbulence sets in. By comparison to numerical calculations, we associate the oscillations with spiral vortex motion, when evolving vortices expand to rectilinear lines.

PACS numbers: 67.57.Fg, 47.32.-y, 67.40.Vs

In superfluid dynamics a longstanding goal has been to account for the formation of all vortices. A quantized vortex line is a topologically stable structure of a coherent order parameter field, with fixed circulation of superflow. What is then the mechanism by which sudden burst-like turbulent vortex proliferation is started from one single vortex loop which is evolving in applied flow? The common view holds that turbulence, once started, is sustained via loop formation and reconnections, as seen in well-developed thermal counterflow turbulence of superfluid ^{4}He-II [1]. However, as emphasized by Schwarz [2], to start turbulence, for instance in linear flow along a circular pipe, vortices have to be pinned in "vortex-mill" configurations which continuously inject new vortex loops downstream in the applied flow. Nevertheless, a turbulent burst of vortex formation is observed to evolve from a single seed vortex loop in rotating ^{3}He-B, with no permanently pinned vortices [3].

A recent explanation [4] of this controversy concludes that a vortex evolving in applied flow may become unstable while interacting and reconnecting with the container wall. In ^{3}He-B this *single-vortex instability* becomes possible with decreasing temperature below an onset temperature T_{on}, where mutual friction damping has dropped to sufficiently low value: $\alpha(T) \lesssim 1$. In the rotating cylinder the instability leads to a sudden transition to the equilibrium vortex state. This process is most conveniently studied in the onset temperature regime $T \sim T_{on}$, by monitoring the number of vortex lines as a function of time at constant rotation velocity, as a response to the injection of a seed vortex [5]. The events following the instability have been reviewed in Refs. [6, 7] for the case of a long rotating column. Here the end point of an evolving seed vortex describes a spiral trajectory along the cylinder wall while it expands towards its stable state as rectilinear vortex line. In the onset region $T \sim T_{on}$, the spiral vortex motion is sometimes observed to give rise to an oscillating NMR absorption signal which is examined in this report.

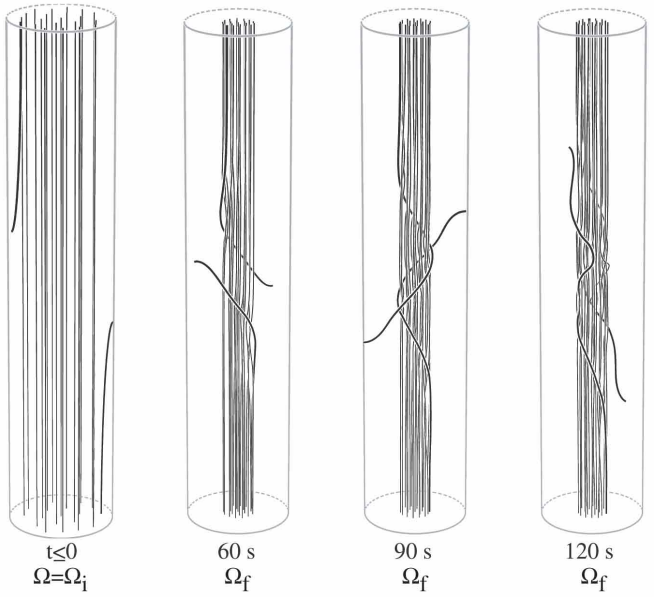

FIG. 1: Numerical calculation of vortex evolution in a rotating cylinder of ^{3}He-B: Rotation is suddenly increased at $t = 0$ from $\Omega_i \approx 0.03$ rad/s to $\Omega_f = 0.2$ rad/s. There are 22 vortices in this sample, of which two in the outermost ring (lying opposite to each other) have been initially bent to the cylindrical wall, to break cylindrical symmetry. In the later snapshots at Ω_f, the two short vortices expand towards the top and bottom end plates of the cylinder, while other vortices have contracted to a central vortex cluster. Parameters: $R = 3$ mm, $L = 30$ mm, $P = 29.0$ bar, and $T = 0.4\,T_c$ (which corresponds to $\alpha = 0.18$ and $\alpha' = 0.16$ [8]).

Numerical illustrations: To visualize the motion of evolving vortices in rotating flow, a calculation is presented in Fig. 1 using the vortex filament method described in Ref. [5]. The initial configuration in Fig. 1, with two curved vortices which connect at one end to the cylindrical side wall, mimics the equilibrium vortex state in a real rotating experiment. Depending on the rotation velocity Ω_i and the residual misalignment between the rotation and the sample cylinder axes ($\lesssim 1^\circ$ in the setup

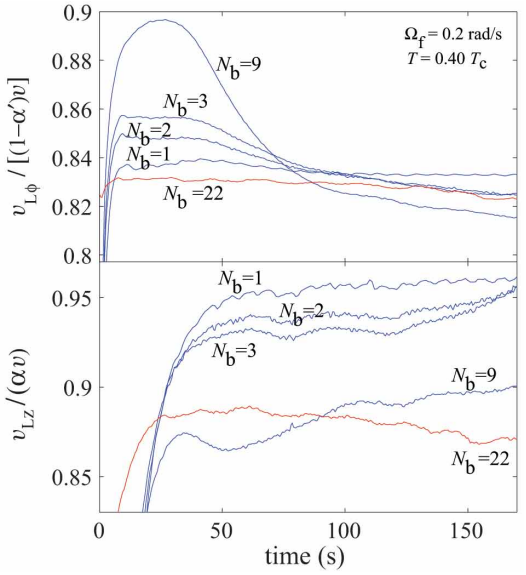

FIG. 2: Comparison of azimuthal $v_{L\phi}$ (top) and longitudinal v_{Lz} (bottom) velocities when different numbers of $2N_b$ vortices expand in the setup of Fig. 1. With 22 vortices in total, 1, 2, 3, or 9 vortices of equal initial length $0.4\,L$ have been bent both on the top and bottom to the cylindrical wall, to mimic a tilted cylinder, as shown in Fig. 1. The spiralling motion both upwards and downwards along the rotating column is calculated as a function of time. The average velocity of the vortex ends on the cylindrical wall in the upward and downward moving bundles is plotted during the time needed to reach the respective end plate. The actual velocity is the number on the vertical scale times $\alpha v(\Omega_f, R, N)$ or $(1-\alpha')v(\Omega_f, R, N)$, where $N = 22 - N_b$. The case $N_b = 22$ is different: here all 22 vortices are initially bent at one cylinder end to the wall and, after the rotation increase to Ω_f, a vortex front starts expanding towards the other vortex-free end of the cylinder. This situation is examined further in Fig. 3.

of Fig. 5), a certain fraction of the peripheral vortices ends on the cylindrical wall [9].

In Fig. 1, rotation is increased in step-like manner at $t = 0$ from the equilibrium vortex state at $\Omega_i \neq 0$ to a final stable value Ω_f. The $N = 20$ rectilinear vortices are thereby compressed to a central cluster with an areal density $n_v = 2\Omega_f/\kappa$ by the surrounding counterflow (cf) at the velocity $\boldsymbol{v} = \boldsymbol{v}_n - \boldsymbol{v}_s$, the difference between the velocities of the normal and superfluid fractions. The highly viscous normal component we consider to be in solid-body rotation: $\boldsymbol{v}_n = \boldsymbol{\Omega}\times\boldsymbol{r}$. Outside the compressed cluster the cf velocity is then given by

$$v(\Omega_f, r, N) = v_n - v_s = \Omega_f r - \frac{\kappa N}{2\pi r}\,, \qquad (1)$$

where $\kappa = h/(2m_3)$ is the quantum of circulation. The two short vortices now expand in this cf in spiral motion towards the top and bottom end plates, respectively. The velocity $\mathbf{v}_L$ of a vortex line element with tangent $\hat{\mathbf{s}}$ is obtained from the equation of motion [10]

$$\boldsymbol{v}_L = \boldsymbol{v}_s + \alpha\hat{\mathbf{s}}\times(\boldsymbol{v}_n - \boldsymbol{v}_s) - \alpha'\hat{\mathbf{s}}\times[\hat{\mathbf{s}}\times(\boldsymbol{v}_n - \boldsymbol{v}_s)]\,, \quad (2)$$

where α is the dissipative and α' the reactive mutual friction coefficient. Since the vortex end is perpendicular to the cylindrical wall, it has from Eq. (2) a longitudinal velocity $v_{Lz} = \alpha v(\Omega_f, R, N)$ and an azimuthal component $v_{L\phi} = (1-\alpha')v(\Omega_f, R, N)$. In the rotating coordinate system, $v_{L\phi}$ points in the opposite direction from the rotation of the container. The resulting end point motion gives us a simple picture of the spiral trajectories along the cylindrical wall, although other parts of the vortex also contribute to its motion, in particular its curvature where it connects to the cylindrical wall. During their expansion the two evolving vortices are wound around the central vortex cluster as a helix whose pitch depends on the cf velocity $v(\Omega_f, R, N)$. Ultimately, the helix will unwind, when the vortex ends slip along the flat end plates of the cylinder, so that the final state is composed of only rectilinear vortex lines. However, since the cf velocity is close to zero at the border of the cluster, the unwinding is a slow process.

The calculated velocities of the vortex ends in Fig. 1 are $v_{Lz} \approx 0.84\,\alpha\Omega R \approx 0.96\,\alpha\, v(\Omega_f, R, N)$ and $v_{L\phi} \approx 0.73(1-\alpha')\Omega R \approx 0.83(1-\alpha')\,v(\Omega_f, R, N)$. The wave length of the spiral trajectory is thus $\lambda = 2\pi R\, v_{Lz}/v_{L\phi} \approx 5\,\mathrm{mm}$ and the period $p = 2\pi R/v_{L\phi} \approx 50\,\mathrm{s}$. In Fig. 2 the spiral vortex motion is analyzed further for the same experimental setup as in Fig. 1, but when several vortices are expanding simultaneously. The initial starting state for these calculations is one where a specified number (N_b) of nearest-neighbor vortices is bent to the cylindrical wall at the same distance of $0.4\,L$ from the end plate both at the bottom and top of the cylinder, similar to the configuration in Fig. 1 (at $t = 0$). When rotation is increased from Ω_i to Ω_f, one set of N_b curved vortices starts expanding towards the top and one towards the bottom end plate. The axial (bottom panel) and azimuthal velocities (top panel) have been plotted as a function of time, for different numbers of $2N_b$ vortices in spiral expansion.

Two observations can be made from Fig. 2. The vortices, which expand in one direction and initially start off in close proximity of each other, remain a close bundle during their spiral motion. Vortex bundling is a general phenomenon which gives rise to the formation of larger eddies, similar to the eddies in classical viscous fluid motion. Here the bundles do not disperse, but are well preserved especially during the later part of the expansion in a state of steady propagation, since all N_b vortices travel roughly at the same speed both axially and azimuthally along the cylinder. Thus the spread in velocities among the different vortices within the bundle and also the changes in the velocities as a function of time remain relatively small. The second note about Fig. 2 is that both v_{Lz} and $v_{L\phi}$ are rather insensitive to the number of vortices spiralling in the bundle. This is because the total number of vortices $N = 22$ corresponds here to a very low equilibrium rotation velocity $\sim 0.03\,\mathrm{rad/s}$ compared to the actual rotation velocity of $0.2\,\mathrm{rad/s}$. For

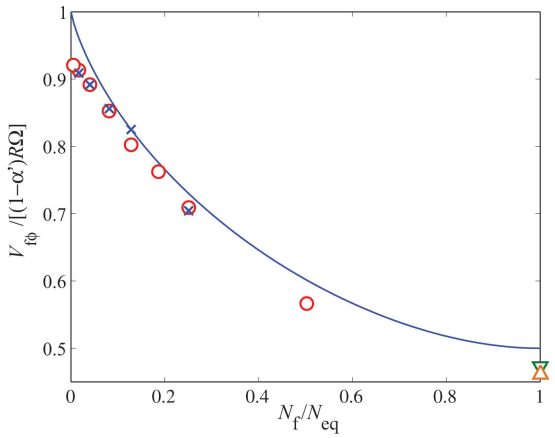

FIG. 3: Calculated azimuthal front velocity $V_{f\phi}$ (in the rotating coordinate system), as a function of the number of vortices N_f which compose the front. No prior vortex cluster exists in the center of the cylinder. The zero temperature limit of Eq. 3 *(solid curve)* is compared to calculations at finite temperatures *(data points)*. The calculations with $N_f < N_{eq}$ are for $R = 3\,\mathrm{mm}$, $L = 30\,\mathrm{mm}$, $\Omega = 0.2\,\mathrm{rad/s}$, where $N_{eq} \approx 170$ vortices: ($\circ$) $\alpha = 0.1$, $\alpha' = 0$; ($\times$) $\alpha = 0.18$, $\alpha' = 0.16$, $T \approx 0.4\,T_c$. The two calculations with $N_f \approx N_{eq}$ are for $R = 1.5\,\mathrm{mm}$, $L = 40\,\mathrm{mm}$, $\Omega = 1\,\mathrm{rad/s}$, where $N_{eq} \approx 210$ vortices: ($\triangledown$) $\alpha = 0.040$, $\alpha' = 0.030$, $T \approx 0.3\,T_c$; ($\triangle$) $\alpha = 0.18$, $\alpha' = 0.16$, $T \approx 0.4\,T_c$. On the vertical scale the normalized velocity $V_{f\phi}/[(1-\alpha')\Omega R]$ is plotted. $V_{f\phi}$ is taken as the front velocity when a stable value has been reached, which generally happens when the front has propagated 2/3 of the length of the cylinder.

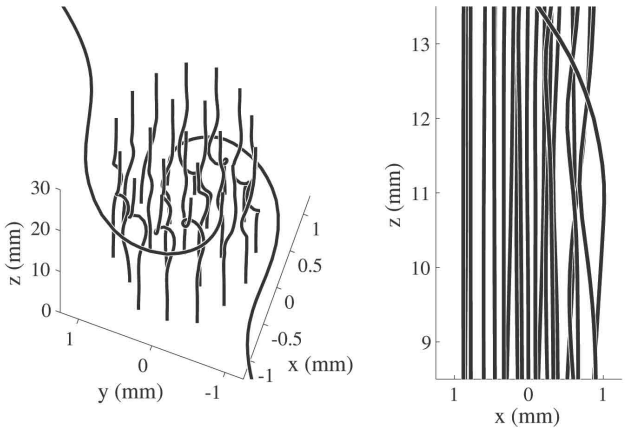

FIG. 4: *(Left)* Rotating vortex cluster from Fig. 1 at $t = 60\,\mathrm{s}$, viewed at an angle deviating by 3° from vertical. Only the central part of the sample cross section in the $x - y$ plane is shown. Helical Kelvin waves are induced on the vortex lines in the cluster by the two vortices spiralling outside the cluster. In the early stage of the expansion, the waves start at roughly half-height of the cylinder, *i.e.* from the points where the two short vortices merge with the cluster (see Fig. 1). *(Right)* Side view through the vortex cluster ($t = 60\,\mathrm{s}$). A vortex spiralling around the cluster induces radial displacements on the outermost vortices within the cluster. The displacements start longitudinally propagating Kelvin waves on these vortices.

better comparison with measurements the final rotation velocity Ω_f should be increased even more, which calls for time-consuming calculations.

A special case is that where all existing vortices are released simultaneously from one end of the rotating cylinder and expand as a vortex front towards the vortex-free end of the cylinder (*i.e.* where no prior central vortex cluster exists). In Fig. 2 this case is the example with $N_b = 22$. Such a calculation models the experimental situation after a turbulent burst, like in Fig. 6 (although there the burst occurs higher up in the column, which then starts both an upward and downward moving front). At temperatures below about $0.45\,T_c$ the front, once it is formed from N_f vortices, maintains its constant narrow width during the spiralling propagation along the column [6, 7]. The longitudinal propagation velocity V_{fz} of the front has been measured and analyzed in Ref. [11]. The azimuthal velocity $V_{f\phi}$ (in laboratory coordinates) is obtained in the continuum model at zero temperature (where friction vanishes) from the equation

$$V_{f\phi} = \frac{\kappa N_f}{2\pi R}\,\frac{1/2\,\ln\left(N_{eq}/N_f\right) + 1/4}{1 - N_f/(2N_{eq})}\,, \qquad (3)$$

where the approximate continuum value for the number of vortices in the equilibrium state is $N_{eq} = \pi R^2(2\Omega/\kappa)$. When $N_f \to N_{eq}$, this expression gives $V_{f\phi} = \frac{1}{2}\,\Omega R$. This limit was discussed in Ref. [12]. In Fig. 3 we compare Eq. (3) to numerical calculations at finite temperatures and finite friction for a few examples. The results for the normalized azimuthal front velocity $V_{f\phi}/[(1-\alpha')\Omega R]$ drop below the estimate from Eq. (3), but by less than 10 %. Thus also at finite friction $V_{f\phi} \approx \frac{1}{2}(1-\alpha')\Omega R$ is a good approximation, which applies when the number of vortices in the front is large ($N \lesssim N_{eq}$).

While spiralling around the cluster in Fig. 1, the two curved vortices may reconnect with each other or with the outermost lines in the cluster. These reconnections do not increase the vortex number. As can be seen from Figs. 1 and 4, a spiralling vortex distorts the cluster by inducing propagating helical Kelvin waves on the vortex lines, which results in oscillations of the cluster around its equilibrium position [13]. The amplitude of the waves is comparable to the inter-vortex distance in the cluster, $\sim 1/\sqrt{n_v}$, and initially the wavelength and period of the excited Kelvin waves have similar values as the precessing vortex motion outside the cluster.

At high friction ($\alpha \geq 0.18$) the number of vortices remains strictly constant in Figs. 1 – 4. At low friction ($\alpha \leq 0.1$) the calculations on the precessing vortex front in Fig. 3 may display some increase in vortex number, when $N < N_{eq}$. Figs. 1 – 2 thus illustrate the situation above T_{on} where no increase in vortex number occurs. Experimentally T_{on} depends on the applied flow velocity ($\sim [\Omega_f - \Omega_i]R$) and on the number ($N_f$) and initial configuration of evolving vortices [5, 7, 14]. In most cases

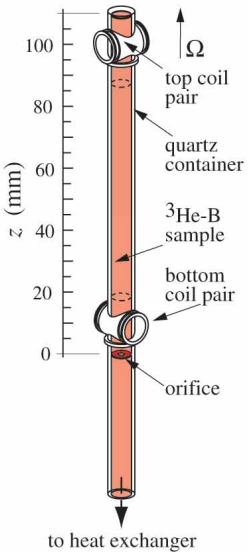

FIG. 5: Sample cylinder with detector coils.

$T_{\rm on}$ is found to be higher than the temperature of the present calculations, $0.40\,T_{\rm c}$. The reason for this difference appears to be the high stability of rotating flow in a circular cylinder, which according to our calculations [5] appears to be a particular characteristic of a cylinder with a circular cross section and ideal wall properties, *i.e.* without surface friction or pinning. The most likely section of an evolving vortex to become unstable is the curved piece ending on the cylindrical wall in the maximum flow $v(\Omega_{\rm f}, R, N)$, while the most stable parts are the sections which reside in low cf close to the central vortex cluster. The extreme case are rectilinear vortex lines in the cluster which are experimentally found to remain stable even in sinusoidally modulated rotation at temperatures $\gtrsim 0.3\,T_{\rm c}$.

Experiment: The sample is cooled in a rotating nuclear demagnetization cryostat at 29 bar liquid pressure within a fuzed quartz cylinder, with radius $R = 3\,$mm and length $L = 110\,$mm (Fig. 5). The number of vortices is measured non-invasively simultaneously at both ends of the long cylinder, by monitoring the NMR absorption line shape. Both NMR detectors consist of circular split-pair coils, with a separation of 9 mm between the coil halves and with their common axis aligned transverse to the cylinder. The coils are wound from superconducting wire and are part of a LC resonator with a Q value of $\sim 1 \cdot 10^4$, coupled to a GaAs MESFET preamplifier located within the cryostat at 4.2 K temperature. Both NMR spectrometers operate independently at constant frequency in an axially oriented polarization magnetic field with a linear sweep. The NMR setup is described in more detail in Refs. [3, 15]

With vortex-free cf, the NMR absorption line shape includes a prominent cf peak which is shifted far from the Larmor frequency, while in the equilibrium vortex state the absorption drops to zero at the location of the cf peak [16]. The height of the cf peak increases with the magnitude of the azimuthal cf velocity $v(\Omega, R, N)$ and thus decreases with the number of vortices N in the central cluster. The correspondence between peak height and vortex number N can be obtained from calculations of the order parameter texture or from measurements. The measurements which we discuss below use remanent vortices [14] as the seeds which evolve in the applied flow after the rotation increase to $\Omega_{\rm f}$. Such a measurement is performed at constant temperature, by first decelerating rotation to zero from a state with a large number of vortices. Zero rotation is then maintained for a period Δt, to allow vortices to annihilate, with the exception of a few remaining dynamic remnants [14]. The final step is to increase Ω at a fixed rate (typically $d\Omega/dt \leq 0.02\,{\rm rad/s^2}$) to $\Omega_{\rm f}$, where it is kept constant while the buildup in the number of vortex lines $N(t)$ in the central cluster is recorded as a function of time.

Single vortex instability: Well above the onset temperature, the cf peak height settles at $\Omega_{\rm f}$ to a stable value and remains constant. Well below onset the cf peak collapses to zero when the equilibrium vortex state is formed. Around the onset temperature $T \approx T_{\rm on}$, both types of behavior occur randomly. If the equilibrium vortex state is here formed, then in perhaps one third of the cases the collapse of the cf peak can be preceded by an initial slow decrease in peak height. The slow reduction in peak height corresponds to slow generation of new vortices. It is the signature of the single-vortex instability, as described and analyzed in Ref. [5]. It can only be observed in the onset regime $T \sim T_{\rm on}$; at lower temperatures the instability proceeds too rapidly to be monitored with our techniques. The slow vortex generation is terminated in a turbulent burst which takes place as a localized event in some short section (of length $\sim R$) of the long sample column. In this burst enough vortices are created to start the evolution towards the equilibrium vortex state. From the site of the burst the vortices propagate in spiral motion as a front both up and down along the cylinder, leaving behind a vortex bundle composed of helically twisted vortices [6, 7].

The NMR absorption responses of rapid and slow transitions to the equilibrium vortex state are compared in Figs. 6 and 7, respectively. These were recorded in two consecutive measuring runs at the same temperature using the same measuring procedure. The order of the two measurements was such that Fig. 7 was measured first and Fig. 6 next. The responses prove to be different owing to the different value of the rotation velocity $\Omega_{\rm f}$, which in turn is caused by the stochastic nature of the remanent vortex injection process: in the former case the waiting period at zero rotation prior to the measurements was $\Delta t = 40\,$min, while in the latter case it was 22 min. Thus in Fig. 6 the remanent vortices are expected to be fewer and smaller loops. In

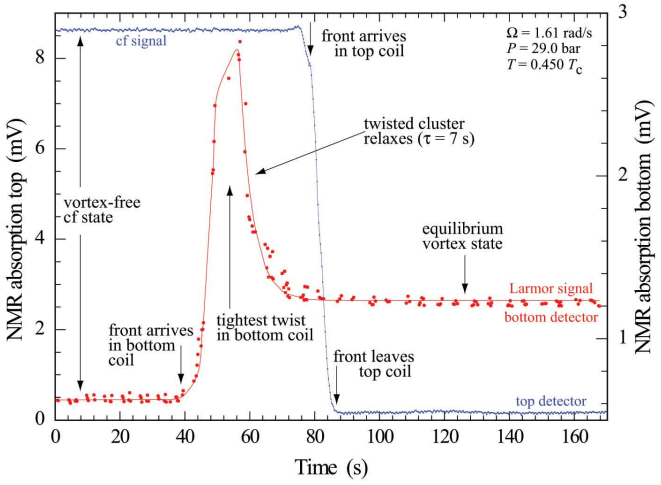

FIG. 6: NMR response during a rapid transition from vortex-free flow to the equilibrium vortex state at constant externally controlled conditions. The top and bottom detectors monitor the NMR absorption at different values of constant NMR field. The cf peak height is recorded with the top detector, while the bottom detector monitors the peak close to the Larmor edge. Time $t = 0$ marks the moment when $\Omega_f = 1.61\,\mathrm{rad/s}$ is reached. The time delay between the sudden rise in the bottom response (at $t = 40\,\mathrm{s}$) and the start of the rapid collapse in the top (at $t = 78\,\mathrm{s}$) is caused by the longitudinal motion of the two vortex fronts along the column, controlled by $\alpha = 0.33$ [8].

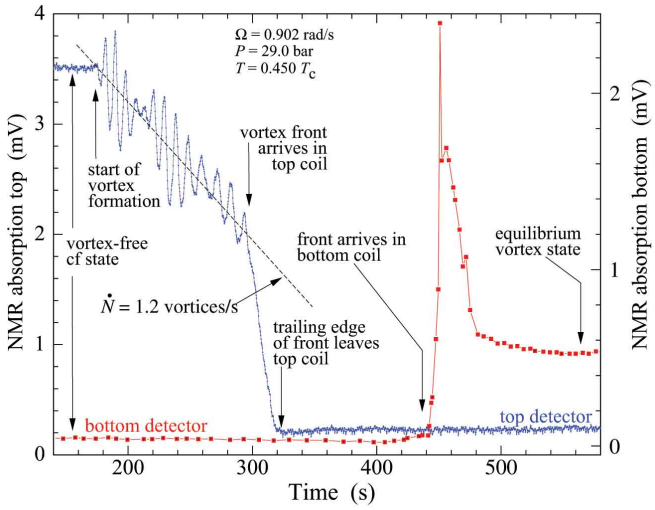

FIG. 7: Precursory vortex formation which terminates in a sudden turbulent burst. This is a repetition of the measurement in Fig. 6, but at a lower rotation velocity $\Omega_f = 0.90\,\mathrm{rad/s}$. The difference is the prolonged slow vortex generation via the single-vortex instability, denoted by the dashed line. Superimposed comes the large-amplitude quasi-coherent oscillation in the cf peak height at a frequency which is related to the azimuthal vortex motion. The latter is controlled by $1 - \alpha' = 0.76$ [8].

both cases the sample was then accelerated to rotation at $\dot{\Omega} = 0.004\,\mathrm{rad/s^2}$. The acceleration was interrupted occasionally, to check at constant rotation whether vortex-free rotation continued to persist over long periods in time. In Fig. 6 (Fig. 7) rotation could be increased until 1.61 rad/s (0.90 rad/s), before any indication of vortex formation was noticed. Time $t = 0$ coincides with the moment when $\Omega_f = 1.61\,\mathrm{rad/s}$ (0.90 rad/s) was reached. After 40 s (170 s) the first response from vortices is observed in the bottom (top) spectrometer. This should be compared with the time it takes for a small vortex loop to expand in vortex-free flow at Ω_f from one end of the cylinder to the other, to become a rectilinear line, $\approx L/(\alpha\Omega_f R) = 70\,\mathrm{s}$ (120 s). In Fig. 7 the start of vortex formation is thus unusual because of the long 170 s delay, before the generation of new vortices starts. The explanation for the long delay must be associated with the properties of a small remanent vortex loop with a radius close to the critical value of $\sim 4\,\mu$m needed to overcome the barrier for spontaneous expansion [17].

Counterflow peak response : In Figs. 6 and 7 the peak heights of two different absorption maxima of the NMR spectrum are recorded as a function of time at constant externally controlled conditions. These are: (1) The cf peak height, which initially in vortex-free flow is at maximum and zero in the final equilibrium vortex state. (2) The Larmor peak height, which initially is close to zero, but in the final state different from zero. While the Larmor peak response is qualitatively similar in the two examples, the drop in the cf peak height happens differently. Fig. 6 shows the generic response from a rapid transition, while in Fig. 7 the decay in the cf peak height starts first with a more gentle linear decrease (dashed line) where the number of vortices gradually increases within the top detector, as generated by the single-vortex instability. This continues for more than 100 s, before the rapid peak height decay starts. (Also in Fig. 6 at higher Ω_f a short vestige of slower peak height reduction can be distinguished, but the rate is faster and it only lasts for $\sim 4\,\mathrm{s}$.) However most importantly, in Fig. 7 the slow decrease in peak height differs from usual examples in that the cf peak height also displays well resolved oscillations of large amplitude. The characterization of these oscillations is the central issue in this report.

According to the measured calibration, the linear decrease in the cf peak height, as marked by the dashed line in Fig. 7, represents a vortex formation rate $\dot{N} \approx 1.2\,\mathrm{vortices/s}$. The later rapid collapse is caused by the arrival of the vortex front [11] to the bottom end of the top coil and its subsequent travel through the coil. At the arrival of the front, the central cluster within the top coil contains ~ 140 vortices (to be compared with $N_{eq} \approx 840$ in the equilibrium vortex state). The front incorporates approximately all the remaining vortices needed to fill the sample with the equilibrium vortex state. The front, composed of these additional vortices, travels in spiral motion along the cylinder around the central cluster. Behind the front the expanding vortices are wound in a heli-

cally twisted configuration which later slowly relaxes [12]. At that point the macroscopic cf, which was generated by the rotation increase to $\Omega_{\rm f}$, is completely removed.

Larmor peak response: The second signal trace in Figs. 6 and 7 is recorded by scanning the absorption maximum close to the Larmor edge with a rapidly moving field sweep. Here the sudden sharp absorption increase signals the arrival of the vortex front, as it passes through the top edge of the bottom detector. The increasing absorption is generated by the axially flowing supercurrent which is produced by the helically twisted vortices behind the front [18]. The subsequent exponential decay of this absorption is caused by the unwinding of the twist while the vortex ends slip along the top and bottom end plates of the sample cylinder and the vortices are converted to rectilinear lines [12]. Thus the Larmor absorption response forms a transient peak, followed by a stable final absorption level, which is representative of the equilibrium vortex state, after the twist has relaxed [6].

In Fig. 7 a delay time $t_{\rm d} \approx 144\,$s separates the moments when the vortex fronts moving up and down along the column pass through the bottom edge of the top detector and the top edge of the bottom detector, respectively. This distance is 82 mm. The longitudinal propagation velocity $V_{{\rm f}z}$ of the front has been measured to be $V_{{\rm f}z}/(\Omega R) \approx 0.28$ at $0.45\,T_{\rm c}$ [11], in a situation when there is no prior central vortex cluster. Assuming that the propagation velocity of the front in the presence of a central vortex cluster is $\approx v(\Omega_{\rm f}, R, N)\ V_{{\rm f}z}/(\Omega R)$, we estimate that, with a vortex formation rate of $\dot{N} \approx 1.2\,$vortices/s, on an average $N \approx 230$ vortices populate the central cluster at the time when the front travels from the location of the turbulent burst to the top edge of the bottom detector. The delay time of 144 s can then be used to localize the site and the moment of the turbulent burst. Here the burst proves to happen a couple of mm below the top detector at $t \approx 290\,$s, or some five seconds before the absorption response in the top detector starts to collapse. In Fig. 6 at a higher flow velocity all events occur faster: with a delay of 33 s between the first bottom and top responses, the burst happens at $t = 28\,$s some 19 mm above the top edge of the bottom coil.

Spiral vortex motion: The generic signal from slow vortex generation in the cf peak height is a relatively smooth decay, while the many periods of well-resolved quasi-coherent oscillation in Fig. 7 are unusual. If both the top and bottom detectors are tuned to monitor the cf peak height simultaneously, then the two recordings of the oscillations look similar, but neither the amplitudes or the frequencies are exactly identical. Since the distribution and number of evolving vortices varies along the column, this is expected. Obviously the oscillating signal is driven by the spiral vortex motion, which is the only source for precession at a frequency around 0.1 Hz. In Fig. 8 we have extracted the difference in time between the maxima and minima in the oscillation of Fig. 7. This

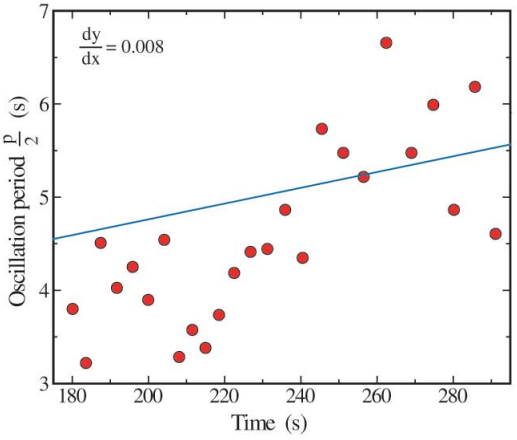

FIG. 8: Time difference between the maxima and minima in the oscillating cf peak height in Fig. 7. The line is obtained by inserting the appropriate values from Fig. 7 in Eq. (4).

data set consists of 13 full periods. The average period is 9.2 s, but the period also appears to be increasing with time. The spiral vortex motion is expected to have the frequency

$$f_\phi = \varepsilon\,(1-\alpha')v(\Omega_{\rm f}, R, N)/(2\pi R)\ , \qquad (4)$$

so that $\dot{f}_\phi \propto -\dot{N}$. We assume that the azimuthal vortex velocity is of the form $v_{{\rm L}\phi} = \varepsilon(1-\alpha')v(\Omega_{\rm f}, R, N)$, where $\varepsilon < 1$ is a numerical factor, which in the case of Fig. 2 is about 0.8. The measuring setup in Fig. 5 incorporates also an instrument factor: The sensitivity of the detector coil pair is not constant across the cross section of the sample, but increases towards the windings. The cf peak height is regulated by the azimuthal vortex-free flow, *i.e.* the height depends on the velocity $v(\Omega_{\rm f}, R, N)$ at the cylindrical wall. This doubles the frequency of an azimuthally precessing asymmetry in the cf velocity $v(\Omega_{\rm f}, R, N)$. For simplicity we assume that $\varepsilon = \frac{1}{2}$ which then compensates for the frequency doubling owing to the sensitivity pattern.

If we take $\dot{N} \approx 1.2\,$vortices/s and $N = 0$ at the moment when vortex formation starts (at $t = 170\,$s) in Fig. 7, we obtain the line through the data in Fig. 8. The best fit would have a twice larger slope, but in view of the large scatter in the signal, which is only quasi-coherent, the agreement with the calculated line appears acceptable. Using this approach, we have extracted $1-\alpha'$ from seven runs with slow oscillatory cf peak decay. In these seven cases the single-vortex instability proceeds at a rate $\dot{N} \sim 0.4$ — 2 vortices/s, while $\Omega_{\rm f}$ is in the range 0.8 — 1.2 rad/s. As seen in Fig. 9, the results agree with the measurements on $1-\alpha'(T)$ in Ref. [8].

Discussion: The oscillatory response in the cf peak height in Fig. 7 is a rare event where several preconditions seem to be fulfilled:

1) New vortices have to be created at a slow rate $\dot{N} \sim 1$, which requires that $T \approx T_{\rm on}$.

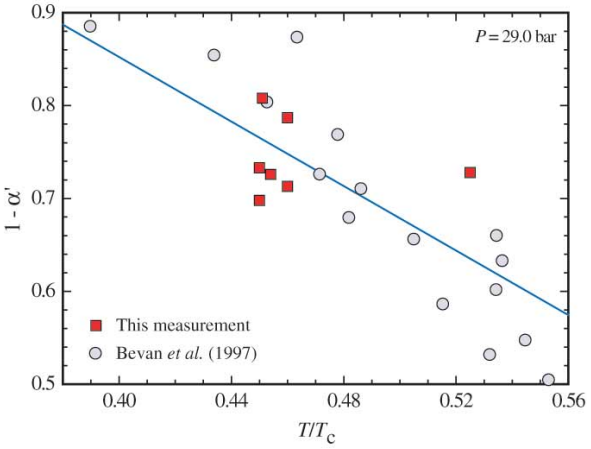

FIG. 9: Consistency test on the analysis of the cf peak height oscillations from seven different measuring runs. The reactive mutual friction coefficient $1 - \alpha'$ has been extracted using Eq. (4) and is compared to the measurements in Ref. [8]. The line is a fit from Ref. [8].

2) In all examples the longitudinal vortical transit time through the 9 mm long detector coil pair is roughly 10 s and equal to the oscillation period in the cf peak height.

3) The oscillations start immediately when the slow vortex generation switches on. In Figs. 6 and 7 the resolution in the measurement of N is roughly one vortex, *i.e.* the reduction in cf peak height per one vortex is approximately equal to the amplifier noise (when $N \ll N_{\rm eq}$). This signal/noise resolution applies to the reduction in cf peak height, when one new vortex is placed in the center of the cylinder. Presumably the signal from a single vortex spiralling along the cylinder wall is larger.

4) To explain the quasi-coherent oscillation, the spiral motion of several vortices has to be reasonably coherent: the 13 oscillations in Fig. 7 cannot be attributed to a single vortex since the transit time for a vortex end to pass through the detector coil pair is equal to one period. Three features may help to create and preserve coherence in spiral motion: (i) When a vortex end on the cylindrical wall creates a new loop, one end of the new loop starts spiralling close to the original end. (ii) Both detectors are close to one of the end plates of the cylinder and, assuming that the single-vortex instability occurs randomly everywhere on the cylindrical wall [5], almost all vortices approach the detector from the direction of the far end of the cylinder. (iii) In numerical calculations the evolving vortices, which start to spiral as a close bundle, tend to remain in a bunch while propagating along the cylinder.

A complete explanation has not been worked out for the mechanisms which gives rise to the oscillating signal in the cf peak height. To understand the coherence over many periods of spiral motion we need better agreement between vortex-dynamics calculations and the experiment, in particular concerning the generation of new vortices by the single-vortex instability in a rotating circular cylinder [5]. As to the amplitude of the oscillations, spiral vortex motion gives rise to oscillatory displacements of the order parameter texture from cylindrical symmetry, as seen in Fig. 4. To explain the signal from such oscillations, numerical calculations are needed on distortions of flare-out textures from cylindrical symmetry and on the resulting NMR line shapes.

Conclusions: We have studied the single-vortex instability of evolving vortices in the turbulent temperature regime of ^{3}He-B. In applied flow the single-vortex instability generates new vortices and becomes the precursor mechanism which starts turbulence. In a rotating circular cylinder the instability occurs while remanent vortices, for instance, expand in spiral motion towards their stable state as rectilinear vortex lines. The spiral motion has been examined here with numerical calculations, but we also argued that oscillations in the NMR response bear direct evidence for the precessing motion. Other kinds of oscillating responses from precessing vortex motion have been reported before. A remarkable example is the unwinding of trapped circulation around a thin wire suspended along the axis of a cylindrical container, known as the Vinen vibrating wire experiment [19]. The spiral motion of an evolving vortex around a central cluster of vortex lines provides another example of precessing vortex signals.

Acknowledgements: This work was supported by the Academy of Finland (grants 213496, 124616, 114887), by ULTI research visits (EU Transnational Access Programme FP6, contract RITA-CT-2003-505313), and the ESF research program COSLAB.

[1] W.F. Vinen, J. Low Temp. Phys. **145**, 7 (2007).
[2] K.W. Schwarz, Physica B **197**, 324 (1994).
[3] A.P. Finne, S. Boldarev, V.B. Eltsov, and M. Krusius, J. Low Temp. Phys. **135**, 479 (2004).
[4] A.P. Finne, V.B. Eltsov, R. Hänninen, J. Kopu, M. Krusius, E.V. Thuneberg, and M. Tsubota, Phys. Rev. Lett. **96**, 85301 (2006).
[5] R. de Graaf, R. Hänninen, T.V. Chagovets, V.B. Eltsov, M. Krusius, and R.E. Solntsev, J. Low Temp. Phys. December (2008); preprint arXiv:0708.3003v2.
[6] A.P. Finne, V.B. Eltsov, R. Hänninen, N.B. Kopnin, J. Kopu, M. Krusius, M. Tsubota, and G.E. Volovik, Rep. Prog. Phys. **69**, 3157 (2006).
[7] V.B. Eltsov, R. de Graaf, R. Hänninen, M. Krusius, R.E. Solntsev, V.S. Lvov, A.I. Golov, P.M. Walmsley, Prog. Low Temp. Phys. Vol XVI, ed. M. Tsubota (Elsevier B.V., Amsterdam, December 2008); preprint – arXiv:0803.3225v2.
[8] T.D.C. Bevan, A.J. Manninen, J.B. Cook, A.J. Armstrong, J.R. Hook, and H.E. Hall, J. Low Temp. Phys. **109**, 423 (1997); Phys. Rev. Lett. **74**, 750 (1995).
[9] V.M. Ruutu, J.J. Ruohio, M. Krusius, B. Plaçais, and E.B. Sonin, Physica B **255**, 27 (1998).
[10] R.J. Donnelly, *Quantized Vortices in Helium II* (Cambridge Univ. Press, Cambridge, UK, 1991).
[11] V.B. Eltsov, A.I. Golov, R. de Graaf, R. Hänninen,

M. Krusius, V. L'vov, and R.E. Solntsev, Phys. Rev. Lett. **99**, 265301 (2007); A.P. Finne, V.B. Eltsov, R. Blaauwgeers, Z. Janu, M. Krusius, and L. Skrbek, J. Low Temp. Phys. **134**, 375 (2004).
[12] V.B. Eltsov, A.P. Finne, R. Hänninen, J. Kopu, M. Krusius, M. Tsubota, and E.V. Thuneberg, Phys. Rev. Lett. **96**, 215302 (2006); J. Low Temp. Phys. **150**, 373 (2008).
[13] See movies at http://ltl.tkk.fi/research/theory/twist.html
[14] R.E. Solntsev, R. de Graaf, V.B. Eltsov, R. Hänninen, and M. Krusius, J. Low Temp. Phys. **148**, 311 (2007).
[15] A.P. Finne, S. Boldarev, V.B. Eltsov, and M. Krusius, J. Low Temp. Phys. **136**, 249 (2004).
[16] J. Kopu, R. Schanen, R. Blaauwgeers, V.B. Eltsov, M. Krusius, J.J. Ruohio, and E.V. Thuneberg, J. Low Temp. Phys. **120**, 213 (2000).
[17] V.M.H. Ruutu, Ü. Parts, J.H. Koivuniemi, N.B. Kopnin, and M. Krusius, J. Low Temp. Phys. **107**, 93 (1997); Europhys. Lett. **31**, 449 (1995).
[18] J. Kopu, J. Low Temp. Phys. **146**, 47 (2007).
[19] R.J. Zieve, Yu.M. Mukharky, J.D. Close, J.C. Davis, and R.E. Packard, J. Low Temp. Phys. **91**, 315 (1993); *ibid.* **90**, 243 (1993).

Keywords: quantized vortex, vortex formation, vortex dynamics, vortex instability, mutual friction, transition to turbulence, onset temperature of turbulence, precursor of turbulence